

**Fig. 18.1.** (a) Scattering of a projectile particle 1 on a target particle 2. In the laboratory the target particle is initially at rest,  $p_2 = 0$ . In the center-of-mass system (CMS) the particles have initially equal and opposite momenta,  $p_1^* = -p_2^*$ . For elastic scattering, considered here, the momenta are also equal and opposite after the scattering process,  $p_1'^* = -p_2'^*$ . (b) Sodium atoms scattered on mercury atoms, (c) neutrons on lead nuclei, (d) electrons on oxygen nuclei, and (e)  $\pi$  mesons on protons. The differential cross section  $d\sigma/d\Omega$  for the elastic scattering of two particles is given as a function of the CMS scattering angle  $\vartheta^*$ . The laboratory kinetic energy  $E_{\text{kin}}$  of the projectile is given on each figure. For part b the ordinate is a linear scale given in arbitrary units. For parts c, d, and e it is a logarithmic scale given in square centimeters per steradian. *Sources:* (b) From U. Buck and H. Pauly, *Zeitschrift für Naturforschung* **23a** (1968) 475, copyright © 1968 by Verlag der Zeitschrift für Naturforschung, Tübingen, reprinted by permission. (c) From F. Perey and B. Buck, *Nuclear Physics* **32** (1962) 352, copyright © 1962 by North-Holland Publishing Company, Amsterdam, reprinted by permission. (d) From R. Hofstadter, Nuclear and Nucleon Scattering of Electrons at High Energies, reproduced with permission from the *Annual Review of Nuclear and Particle Science*, Volume 7, copyright © 1957 by Annual Reviews Inc. (e) From a conference contribution by J. Orear et al. as reported by G. Belletini, Intermediate and High Energy Collisions, in *Proceedings of the 14th International Conference on High Energy Physics at Vienna* (J. Prentki and J. Steinberger, editors), copyright © 1968 by CERN, Geneva, reprinted by permission.

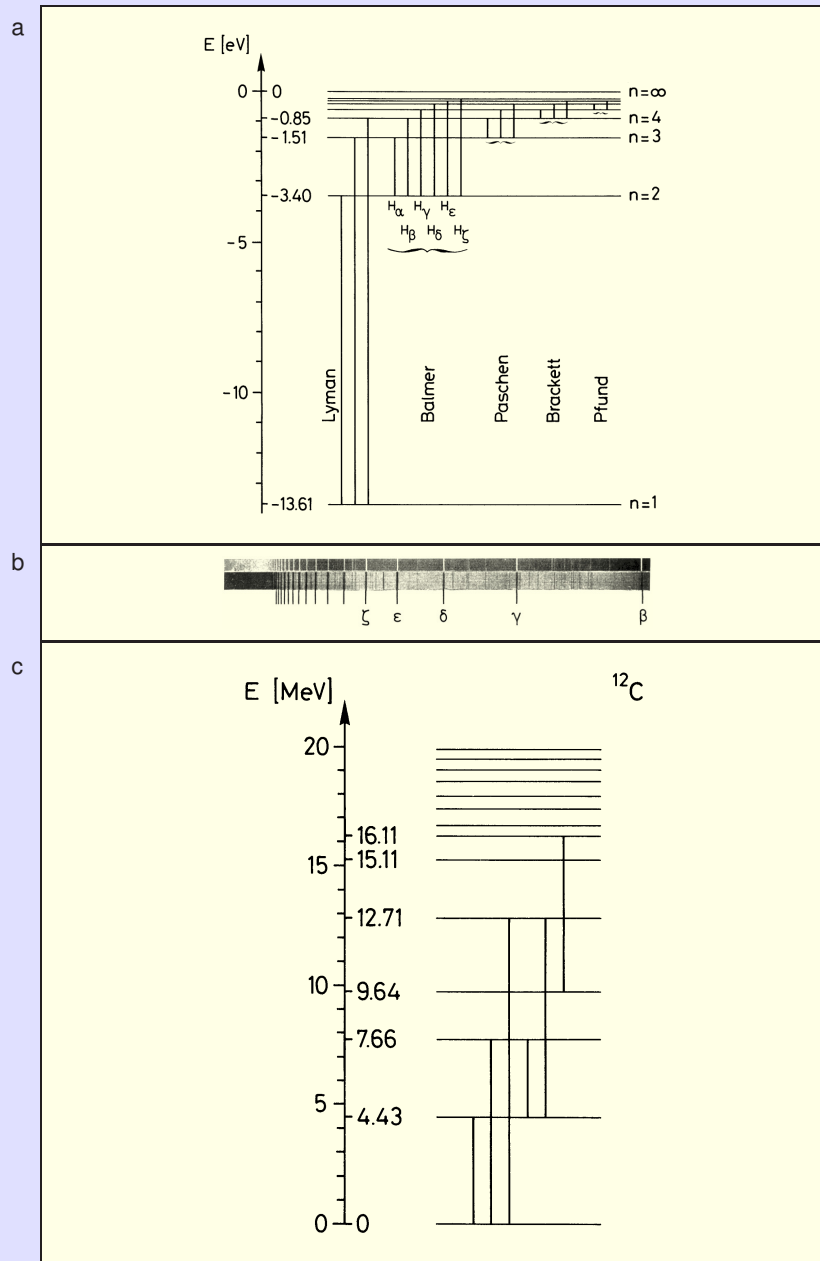


Fig. 18.2. (a) The energy levels that the electron of the hydrogen atom can take are indicated by horizontal lines and enumerated by the principal quantum number  $n$ . Vertical lines indicate the energies at which transitions between different energy levels take place. Transitions to or from the same lower energy level form a series. For example, transitions to or from energy level  $n = 1$  make up the Lyman series. Those to or from energy level  $n = 2$  make up the Balmer series. Transitions to a lower level consist of the emission of a light quantum corresponding to the transition energy. Those to a higher level consist of the absorption of a light quantum. (b) Wavelength spectra of light from different stars show the Balmer series in emission (top) and absorption (bottom). The stars are  $\alpha$  Cassiopeiae and  $\beta$  Cygni. From R. W. Pohl, *Optik und Atomphysik*, ninth edition, copyright © 1954 by Springer-Verlag, Berlin, Göttingen, Heidelberg, reprinted by permission. (c) The different energy levels of the carbon nucleus  $^{12}\text{C}$ . The ground state of the nucleus has been chosen to be the zero point of the energy scale. Some of the observed transitions between energy levels are indicated. These transitions, like those for the hydrogen atom in part a, consist of the emission or absorption of a photon.

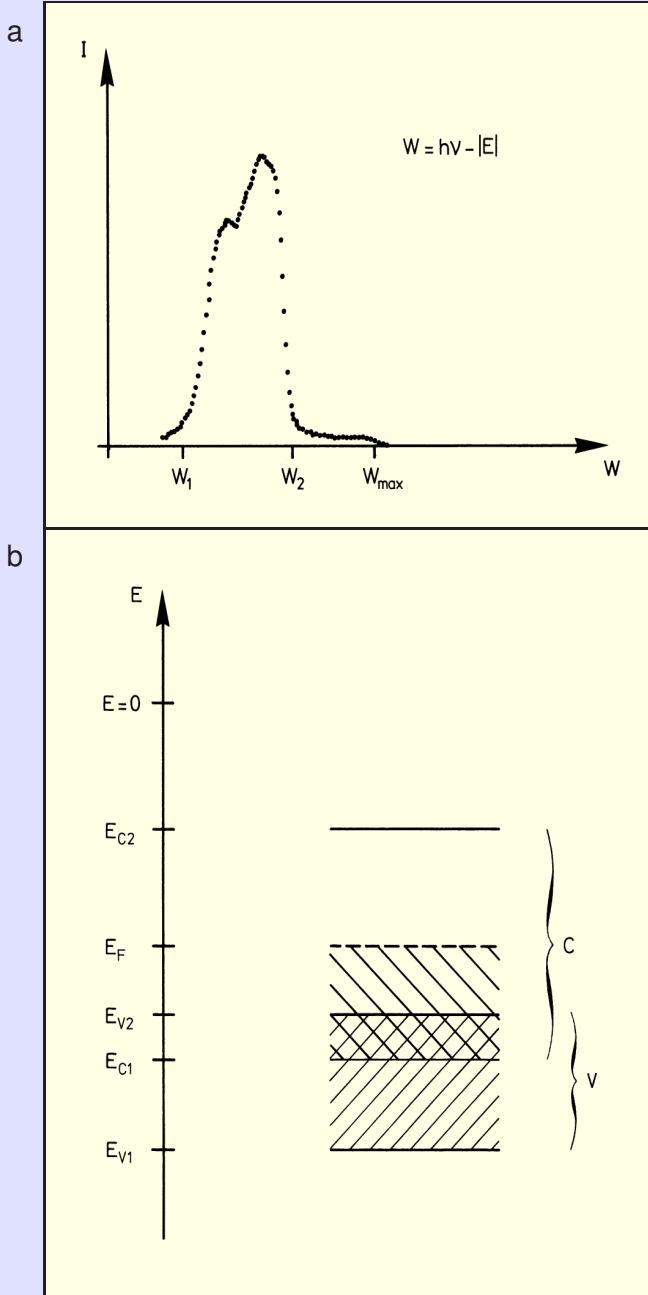


Fig. 18.3. (a) Current  $I$  of photoelectrons emitted by a silver crystal, which has been irradiated by monochromatic X-rays, as a function of the kinetic energy  $W$  of the photoelectrons. By energy conservation we have  $W = h\nu - |E|$ , where  $h\nu$  is the energy of the X-ray photon and  $E$  the energy with which the electron was originally bound in the crystal. Adapted from K. H. Hellwege, *Einführung in die Festkörperphysik*, copyright © 1976 by Springer-Verlag, Berlin, Heidelberg, New York, reprinted by permission. (b) Energy bands of electrons in the silver crystal shown schematically. The conduction band  $C$  is only partly filled with electrons, indicated by the hatched area. The valence band  $V$ , which is completely filled, partly overlaps with the conduction band. Photoelectrons with the highest energy originate from the region of highest energy in the conduction band, that is,  $W_{\max} = h\nu - |E_F|$ .

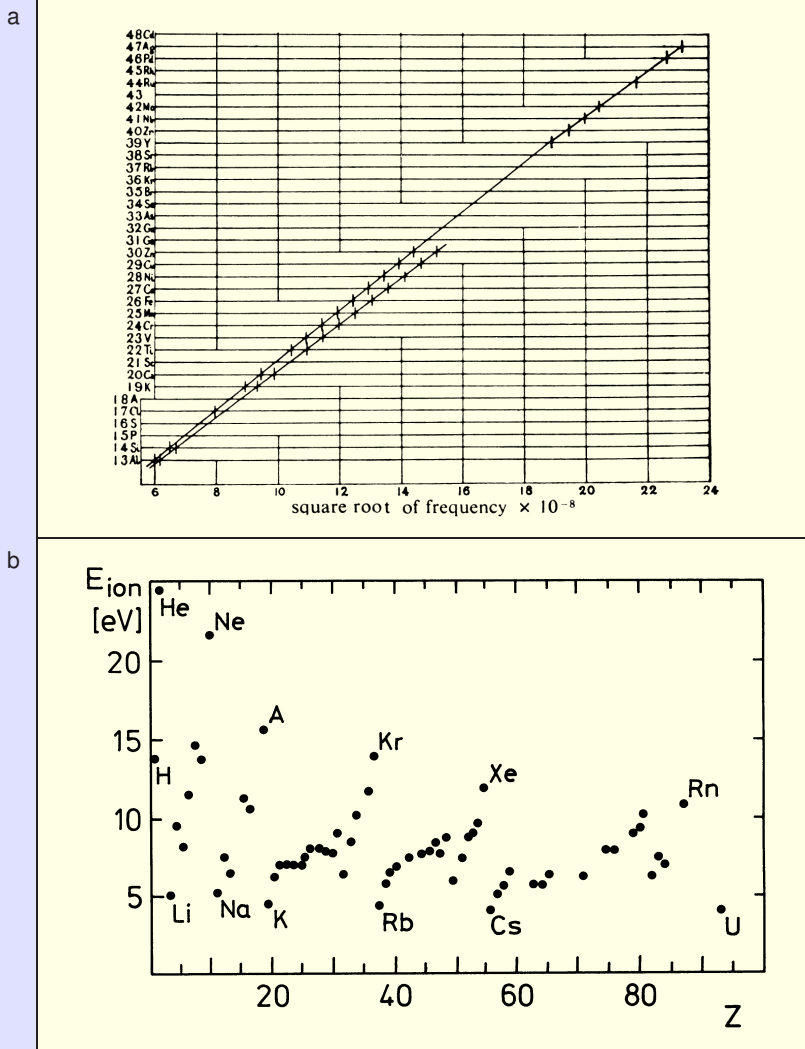
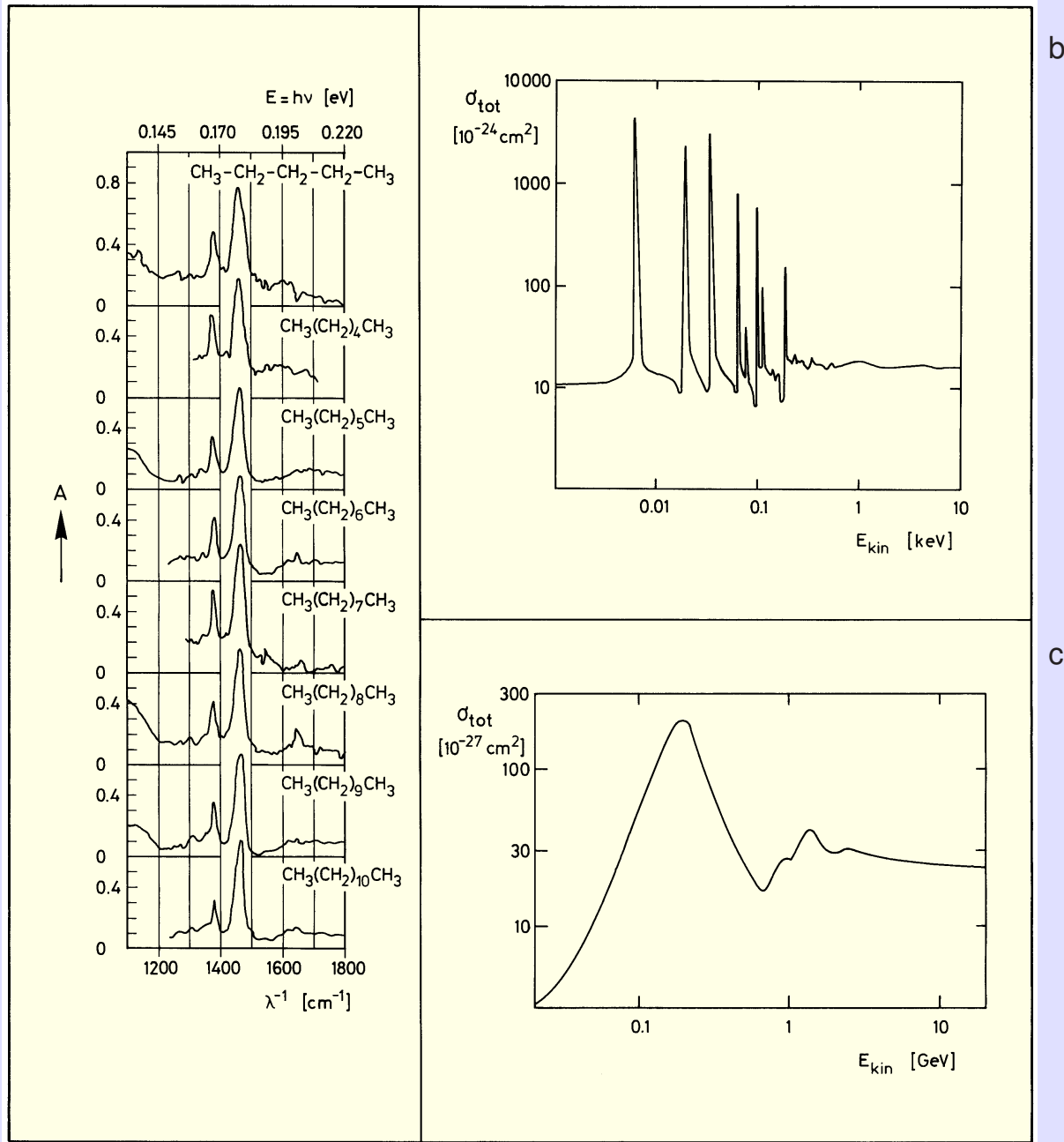
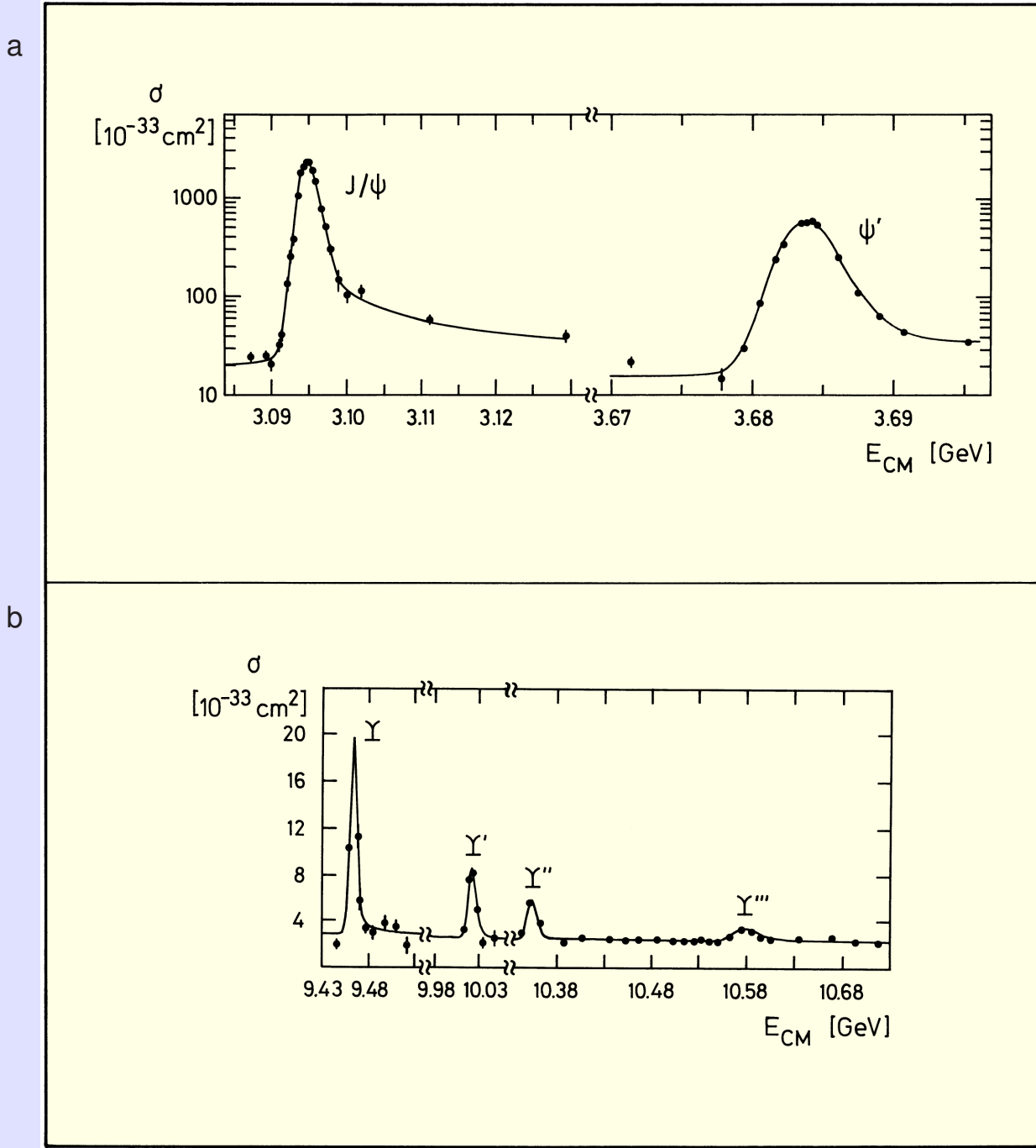


Fig. 18.4. (a) Moseley's plot showing the square root of the X-ray frequency versus the atomic number  $Z$  for  $K_\alpha$  radiation,  $n_2 = 2$  (upper line), and for  $K_\beta$  radiation,  $n_2 = 3$  (lower line). From H. G. J. Moseley, *The Philosophical Magazine* **27** (1914) 703, copyright © 1914 by Taylor and Francis, Ltd., London, reprinted by permission. (b) Ionization energies for atoms as a function of the atomic number  $Z$ . The maxima for noble gases, which have closed shells with  $Z = Z_c$  electrons –  $Z_c = 2$  for helium,  $Z_c = 10$  for neon, and so on – are pronounced, and the drop from  $Z = Z_c$  to  $Z = Z_c + 1$  – that is, from helium to lithium, from neon to sodium, and so on – is sharp.



**Fig. 18.5.** Total cross sections for various reactions as a function of the kinetic energy of the incident particle in the laboratory frame. (a) The absorption coefficient  $A$  for infrared light passing through a layer of paraffin 0.02 mm thick. The abscissa is the wave number  $\lambda^{-1} = \nu/c$  (bottom), which is proportional to the energy  $E = h\nu$  of the light quanta (top). A high rate of absorption corresponds to a large total cross section. Thus the graphs can be interpreted as measurements of the total cross sections as a function of energy. Two characteristic resonances near  $E = 0.17$  eV, which are associated with the vibrations of neighboring  $\text{CH}_2$  groups, are present in all paraffins considered. From Landolt-Börnstein, *Zahlenwerte und Funktionen*, sixth edition, Volume 1, part 2 (A. Eucken and K. H. Hellwege, editors), Figure 33, p. 365, Copyright ©1951 by Springer-Verlag, Berlin, Göttingen, Heidelberg, reprinted by permission. (b) Total cross section for neutrons scattered off lead nuclei. There are many resonances at low energies corresponding to the formation of various metastable states of lead isotopes. (c) Total cross section for positive pions scattered on protons. The wide resonance near  $E_{\text{kin}} \approx 0.2$  GeV corresponds to the excitation of the metastable state  $\Delta^{++}(1232)$ .



**Fig. 18.6.** Total cross section observed for the reaction in which an electron ( $e^-$ ) and a positron ( $e^+$ ) annihilate each other to form a number of strongly interacting particles, such as  $\pi$  mesons. The cross section shows very sharp resonances near (a)  $E_{\text{CM}} \approx 3 \text{ GeV}$  and (b)  $E_{\text{CM}} \approx 10 \text{ GeV}$ . Here  $E_{\text{CM}}$  is the total energy in the center-of-mass system, the system in which  $e^+$  and  $e^-$  have equal and opposite momenta. The unexpectedly sharp resonances are interpreted as evidence that metastable states consisting of a quark–antiquark pair have formed. The  $J/\psi$  family of states is composed of a “charm” quark and its antiparticle. The  $\Upsilon$  family of states is a bound system of a “beauty” quark and the corresponding antiquark. Sources: (a) From A. M. Boyarski et al., *Physical Review Letters* **34** (1975) 1357 and from V. Lüth et al., *Physical Review Letters* **35** (1975) 1124, copyright © 1975 by American Physical Society, reprinted by permission. (b) From D. Andrews et al., *Physical Review Letters* **44** (1980) 1108 and **45** (1980) 219, copyright © 1980 by American Physical Society, reprinted by permission.

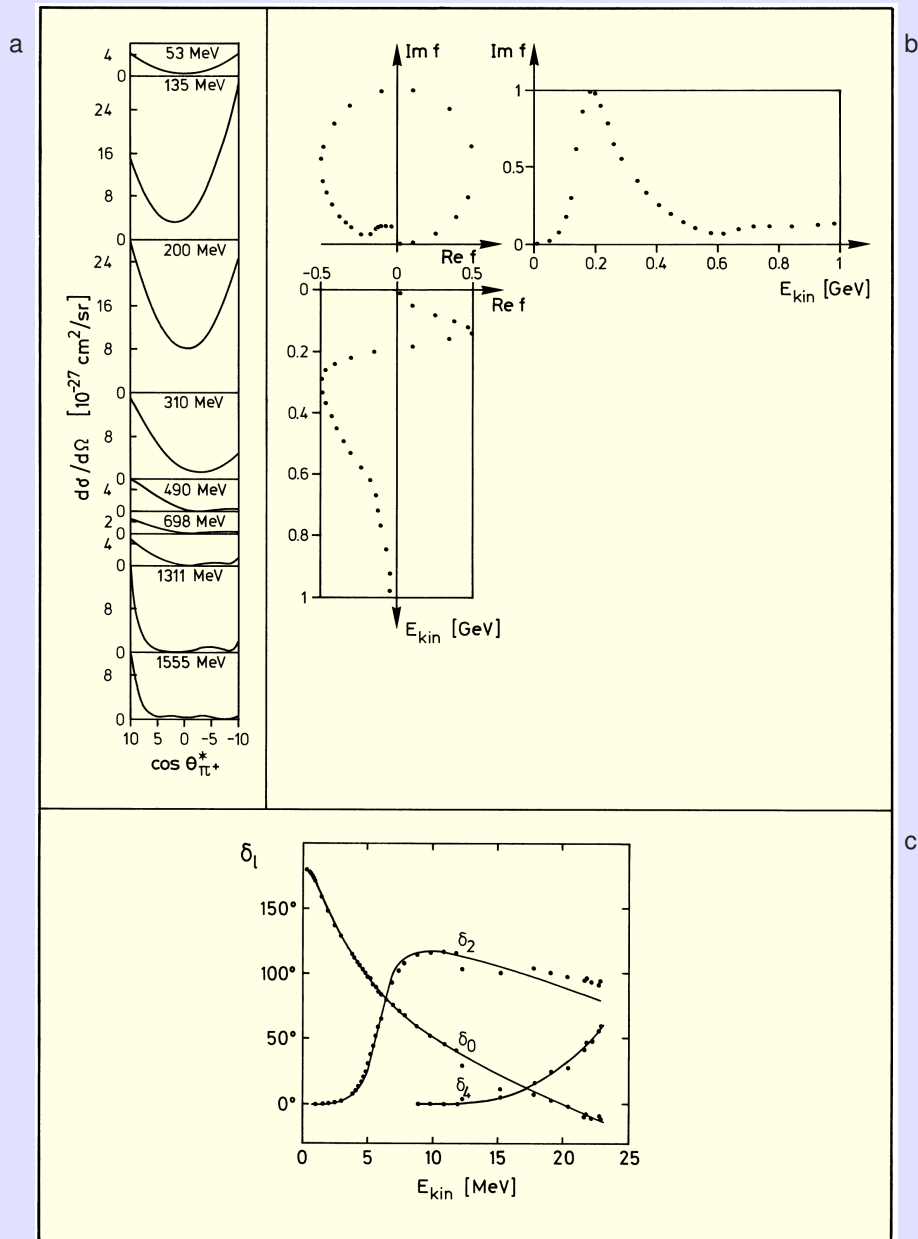


**Fig. 18.7. Phase-shift analysis.** (a) The differential cross section for the elastic scattering of positive  $\pi$  mesons on protons, shown for various kinetic energies of the meson, has a simple parabolic form at  $E_{\text{kin}} = 200 \text{ MeV}$ , indicating a resonance at this energy with angular momentum  $\ell = 1$ . (b) The Argand diagram of the corresponding partial scattering amplitude, reconstructed from measured data. All the features of a resonance at  $E_{\text{kin}} = 200 \text{ MeV}$  are evident. The phase shift passes swiftly through 90 degrees, while the imaginary part goes through a maximum and the real part vanishes. (c) A resonance at much lower energies. Various phase shifts for the elastic scattering of an  $\alpha$  particle on a helium nucleus, that is, another  $\alpha$  particle, are plotted as a function of the kinetic energy of the incoming particle. The resonance in  $\delta_2$  indicates that both particles form a resonance with angular momentum  $\ell = 2$ . Source: (a) From Robert C. Cence, *Pion-Nucleon Scattering*, copyright © 1969 by Princeton University Press, Figure 5.2, p. 62, reprinted by permission of Princeton University Press. (b) Adapted from G. Höhler in Landolt-Börnstein, *Numerical Data*, New Series, volume 9b2 (H. Schopper, editor), Figure 2.2.6, p. 58, copyright ©1983 by Springer-Verlag, Berlin, Heidelberg, New York, reprinted by permission. (c) From T. A. Tombrello and L. S. Senhouse, *The Physical Review* **129** (1963) 2252, copyright © 1963 by American Physical Society, reprinted by permission.

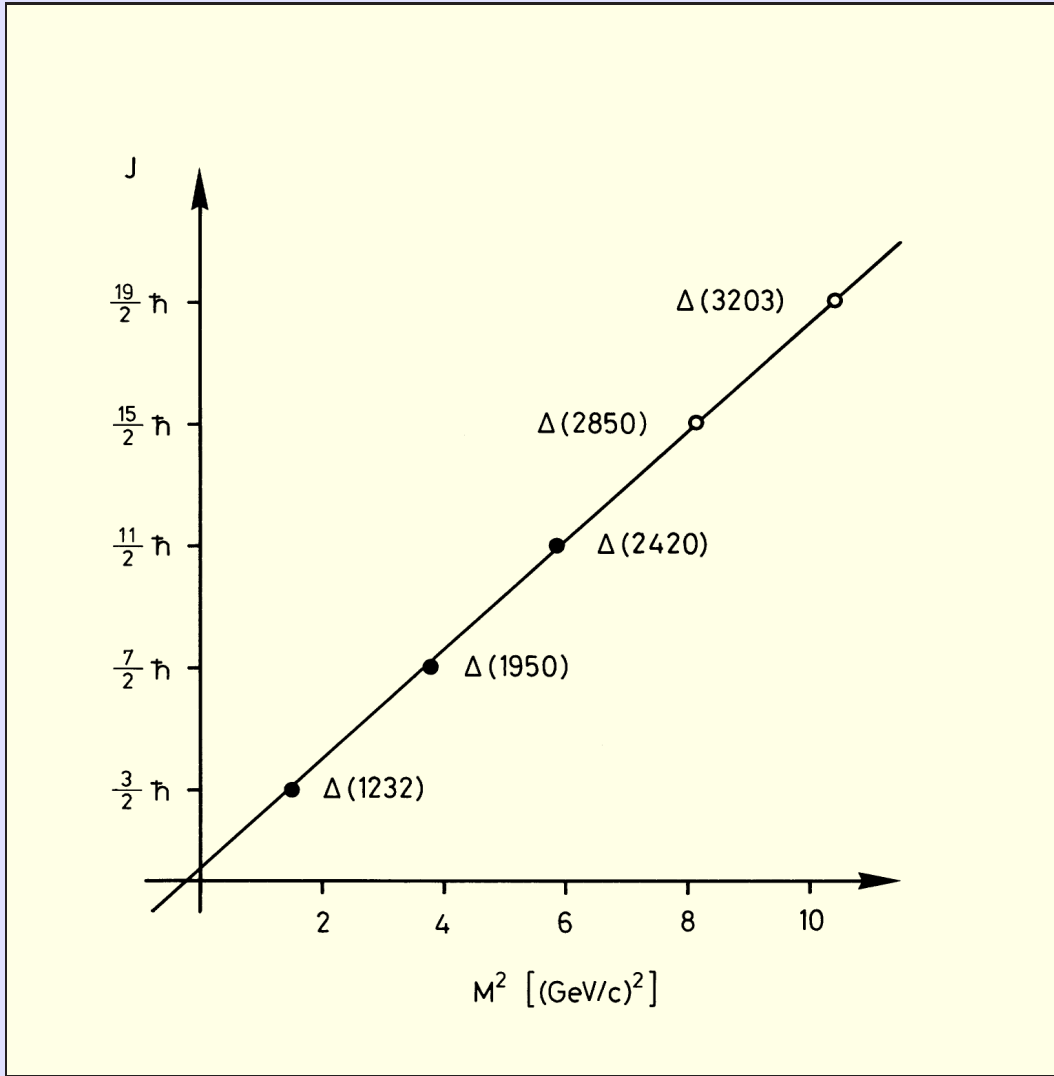
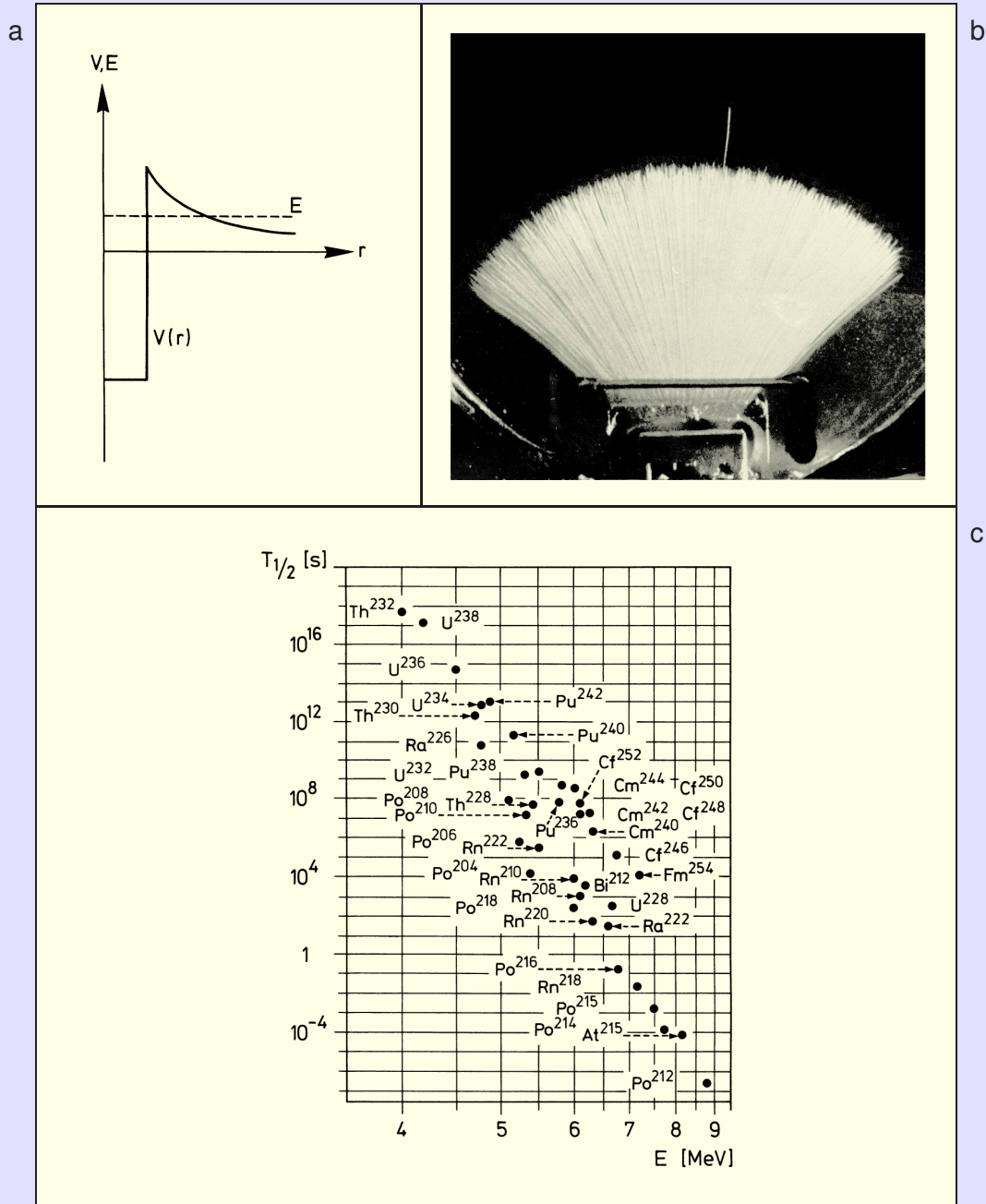
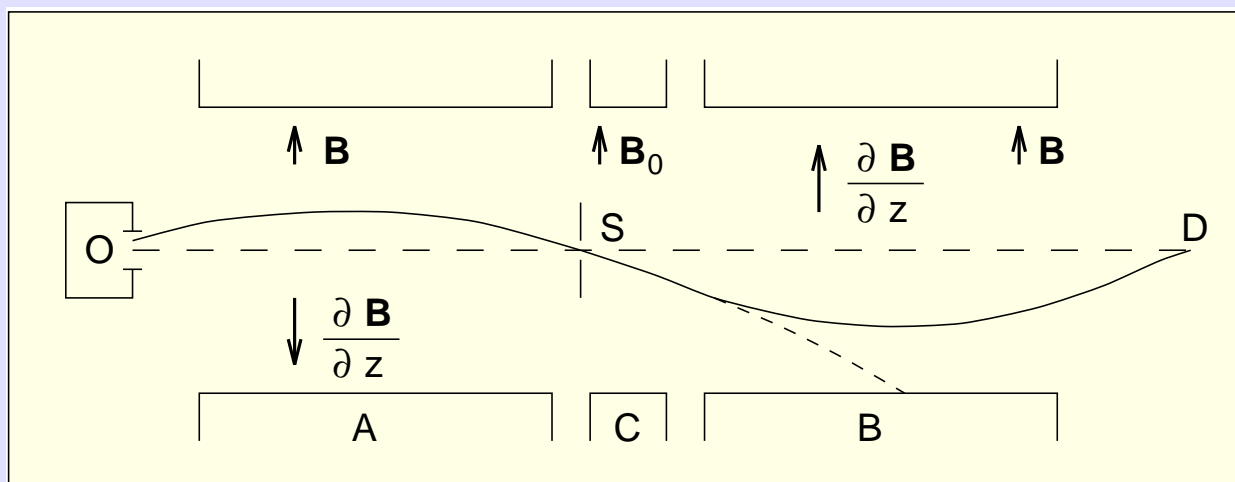


Fig. 18.8. Regge trajectory of the  $\Delta$  particles, which can be understood as resonances formed by a proton and a  $\pi$  meson. The square of the resonance mass  $M^2$  is plotted against the angular momentum  $J$  of the resonance. For the three lowest-lying resonances (black points) both  $M$  and  $J$  have been experimentally determined. For the last two (open circles) only the mass has been measured so far.





**Fig. 18.9.**  $\alpha$  decay. (a) Potential energy  $V(r)$  of an  $\alpha$  particle in a nucleus. Although the total energy  $E$  (dashed line) of an  $\alpha$  particle may be positive, the particle can leave the nucleus only by tunneling through the potential barrier created by the Coulomb attraction between nucleus and  $\alpha$  particle. Therefore metastable states of positive energy can exist. (b) Cloud chamber photograph of tracks of  $\alpha$  particles from the decay of the polonium nucleus,  $^{214}\text{Po}$ . All particles except one have approximately the same range in the chamber gas, indicating that they possess equal energies. The single, long-range track was caused by the decay of an excited state of  $^{214}\text{Po}$  possessing a higher energy. From K. Phillip, *Naturwissenschaften* 14 (1926) 1203, copyright © 1926 Verlag von Julius Springer, Berlin, reprinted by permission. (c) Geiger–Nuttall diagram showing the relation between the half-life  $T_{1/2}$  and the energy of the emitted  $\alpha$  particles for the lowest-lying states of radioactive nuclei. The diagram indicates that the lifetime decreases very rapidly with energy.



**Fig. 18.10.** Rabi apparatus. The magnetic-induction field  $\vec{B}$  points upwards (in the  $z$  direction) in the three magnets A, B, and C. In A and B the field is inhomogeneous, the field gradient  $dB_z/dz$  being negative in A and positive in B. The field in C is homogeneous. For molecules with magnetic moment in  $z$  direction and with momentum within a certain range the trajectory from the source O through the slit S to the detector D is drawn as a solid line. If the direction of the magnetic-moment expectation value is changed to the  $-z$  direction due to magnetic resonance in the additional oscillating field in C the trajectory changes to the broken line and the molecules no longer reach the detector.

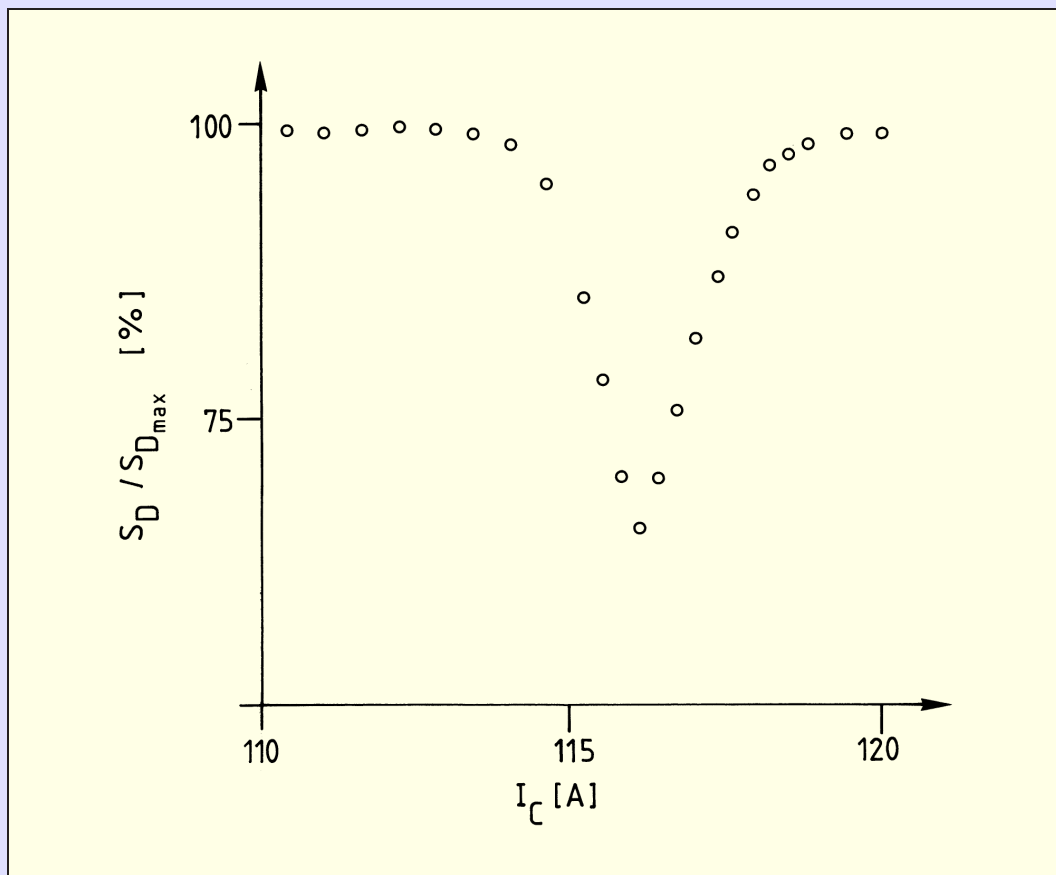


**Fig. 18.11.** Magnetic-resonance curve obtained for LiCl molecules. The signal  $S_D$  in the detector (in percent of the maximum signal) is shown as a function of the current  $I_C$  in the exciting coil of the C magnet and thus the field  $B_0$  while keeping the frequency  $\omega$  of the oscillating field constant. From I. I. Rabi, J. R. Zacharias, S. Millman, and P. Kusch, *Physical Review* **53** (1938) 318, © 1938 by American Physical Society, reprinted by permission.

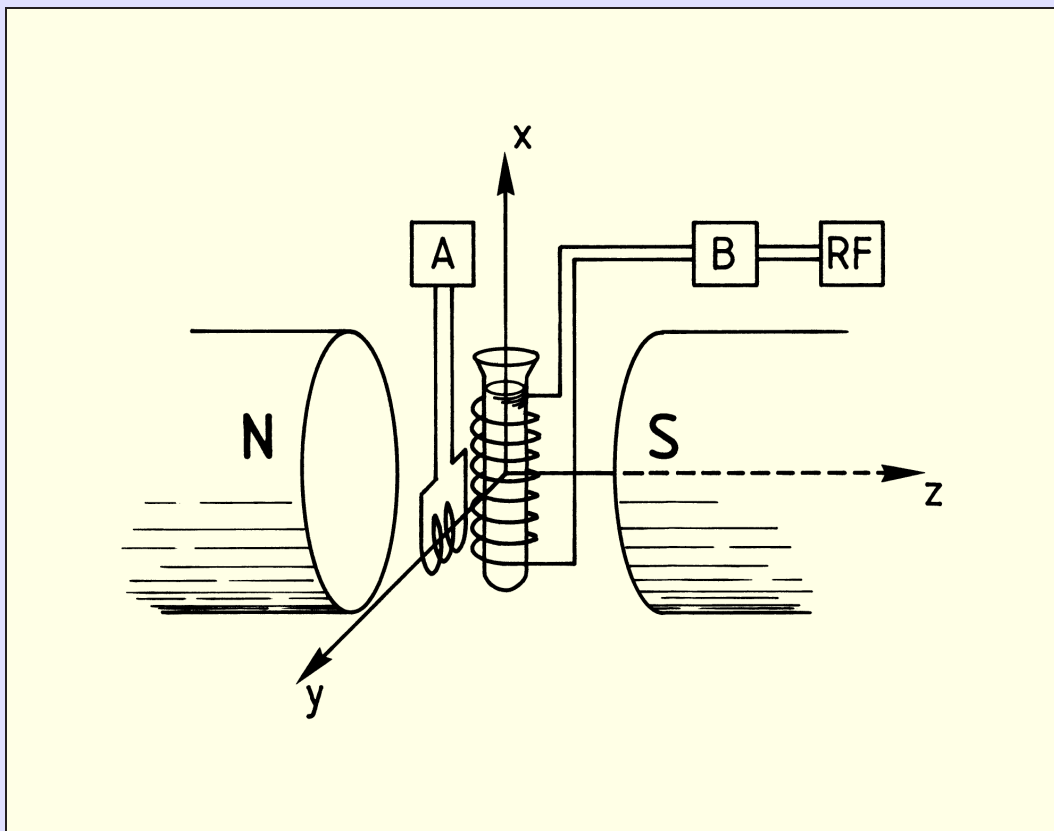
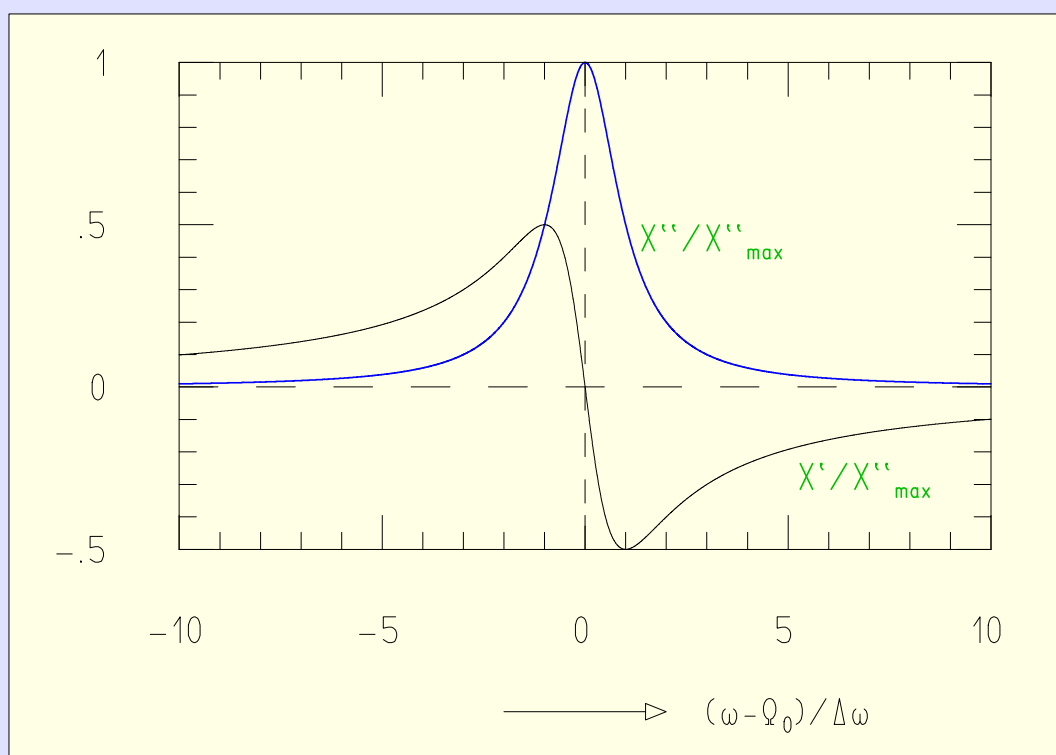


Fig. 18.12. NMR apparatus. An electromagnet (with pole faces N, S) provides a strong homogeneous field  $B_0$  in the  $z$  direction. A coil oriented along the  $x$  direction contains the sample. It is excited by a radio-frequency generator RF of frequency  $\omega$ . The complex resistance of the coil is measured in a bridge circuit B and registered while either  $B_0$  or  $\omega$  are varied. In addition there may be a coil oriented along the  $y$  direction which can pick up magnetic-induction signals from the sample. The signals are amplified by the amplifier A and also registered as a function of  $B_0$  or  $\omega$ .



**Fig. 18.13.** Frequency dependence of the real part  $\chi'$  (thin line) and the imaginary part  $\chi''$  (thick line) of the complex susceptibility.

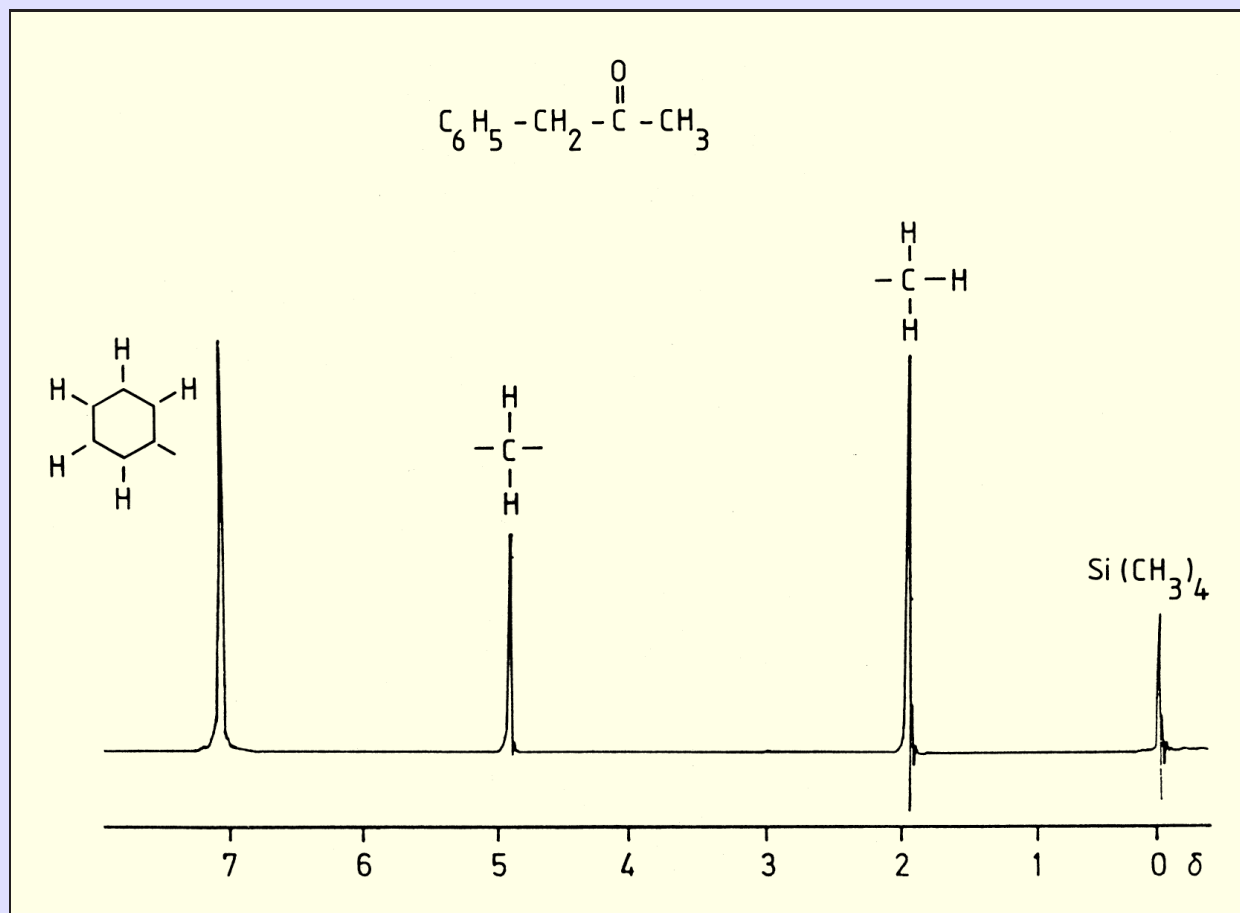
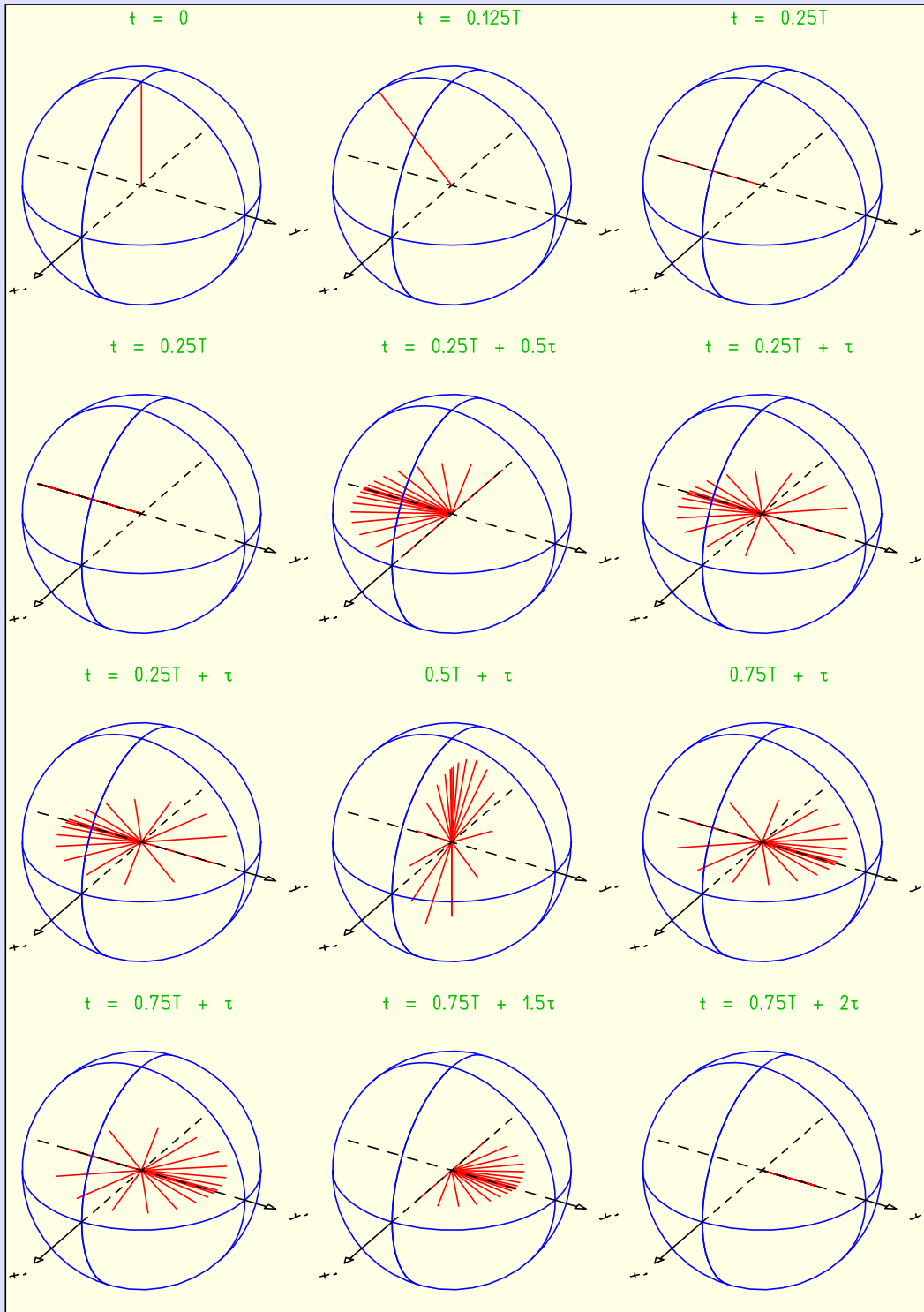
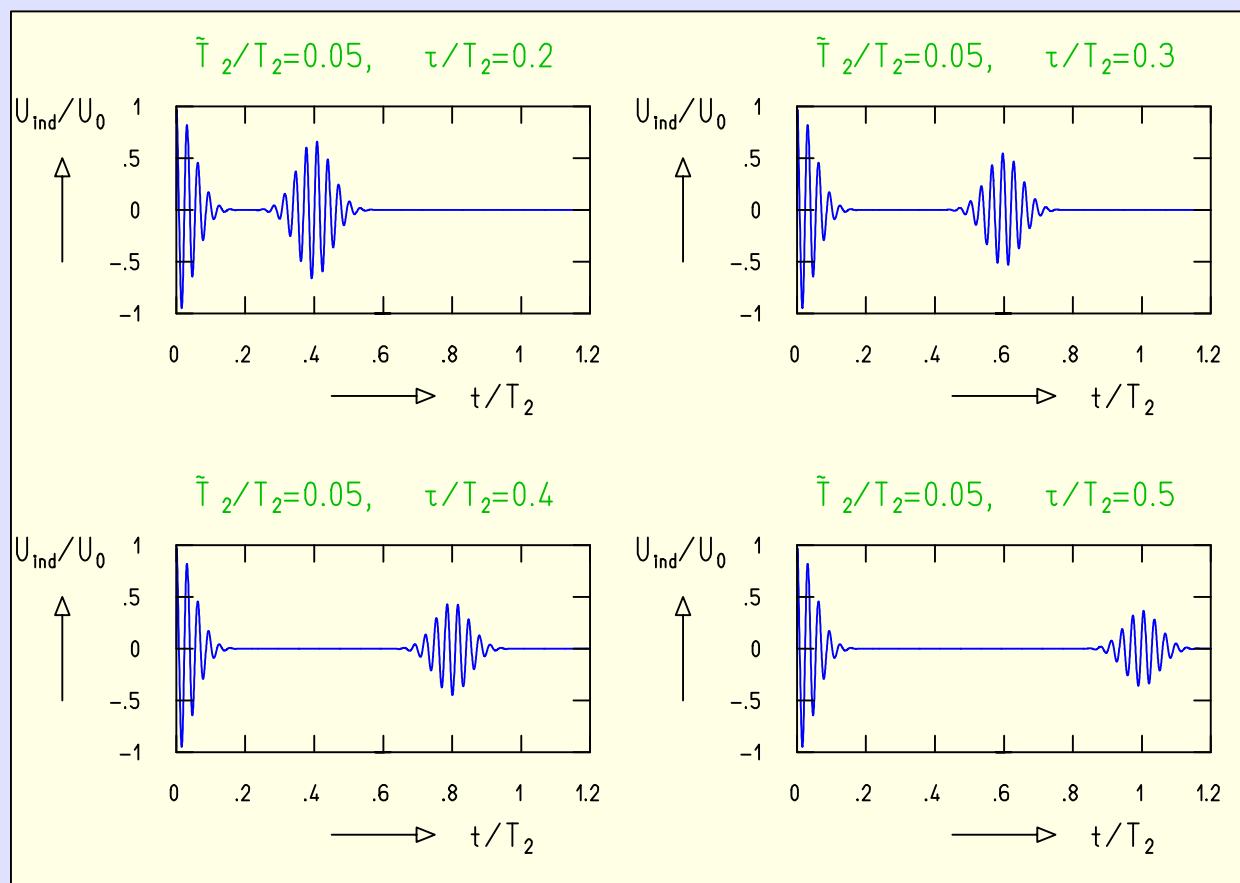


Fig. 18.14. NMR spectrum due to the protons in benzylacetate (first three peaks from the left) in the presence of tetramethylsilane as a reference substance (peak on the far right). On the scale at the bottom of the figure the relative difference of the resonance frequency to the reference peak is given in parts per million (ppm). Adapted from H. Günter, *NMR-Spektroskopie*, 1993 © by Georg Thieme Verlag, Stuttgart, reprinted by permission.



**Fig. 18.15.** Spin echo with  $90^\circ$ – $180^\circ$  pulse sequence shown in the rotating frame of reference. Top row: Application of  $90^\circ$  pulse; local magnetization vectors  $\vec{M}_i$ , initially parallel to each other and to the  $z'$  direction, are rotated onto the  $-y'$  direction. Second row: The  $\vec{M}_i$  get out of phase and spread out in the  $x', y'$  plane. Third row: Application of  $180^\circ$  pulse; each  $\vec{M}_i$  is rotated by  $180^\circ$  about the  $x'$  axis. Bottom row: The  $\vec{M}_i$  back into phase. Because of spin–spin relaxation the magnitudes  $M_i$  of all local magnetization vectors decrease with time.



**Fig. 18.16.** Free induction signal (near  $t = 0$ ) and spin-echo signal at  $t = 2\tau$  for various values of the time  $\tau$  between the applications of the  $90^\circ$  pulse and the  $180^\circ$  pulse.